Dynamic behavior investigation for trajectory control of a microrobot in blood vessels

Laurent Arcese, Ali Cherry, Matthieu Fruchard, Antoine Ferreira

Abstract— This paper reports modeling and control of a microsized polymer aggregate of magnetic particles inside an artery, using a MRI device for supplying propulsion in order to achieve targeted chemotherapy. Non-Newtonian behavior of blood is considered, as well as wall effects and interactions, resulting in a highly nonlinear model. A backstepping approach is synthesized to ensure Lyapunov stability along a pre-planned trajectory inherited from the model, with robustness concerns.

I. INTRODUCTION

Autonomous microrobots designed to perform targeted therapy by navigating in the cardiovascular system are a prolific research area for minimally invasive surgery purposes [1]. Untethered robots are particularly well suited either for reaching remote parts of the body which remain inaccessible to present tools without operating, or for targeting therapy in such places. In the case of chemotherapy, such robots carrying drugs can both improve the therapy's efficiency, reduce drug dose and in turn side effects. As the design of sufficiently powerful embedded actuators for the robot's propulsion is currently a technical challenge on such a scale, wireless transmission of power to the robot using magnetic fields is the more pertinent approach [2], [3].

Bead pulling has first been studied using magnets [4] or superconducting magnets [5]. Recently, Martel has proposed to use the gradients coils of a clinical MRI device to pull the robot [6]. This innovation combines several advantages. Firstly, since medical applications are the purpose of such works, using clinical MRI, widely implanted in hospitals, seems natural. Secondly, these MRI devices can provide both thrust for propelling therapeutic robots and also imaging for a fine localization of the robot inside the cardiovascular system, using multiplexing for controlling and imaging [7].

What is the optimal size for such a robot? On the one hand –from a therapeutic viewpoint– the smaller the better, so as to avoid embolization far from the tumor and to drive the drugs as close as possible to the tumor. On the other hand, since magnetic forces are volumic, they decrease in cubic with size. Besides, partial vessel occlusion by the robot results in an optimal ratio between robot's and vessel's radii evocated in [6]. Along the reference trajectory, from injection point to tumor's area, vessels radius decreases. It is thus necessary to make the robot's radius decrease as it goes in smaller vasculature. This can be done if the robot is a degradable polymer binded aggregate of magnetic particles.

This paper deals with both modeling and controlling such a robot along a reference trajectory. This contribution mainly relies on defining a precise forces balance (Section II), which includes wall effects (parabolic profile of blood flow, pulsatile arterial walls and effect of the ratio of robot's on vessel's radii), wall interactions (Van der Waals, contact and electrostatic forces) and non-Newtonian behavior of blood. The goal is not only to describe the robot's behavior accurately, but also to make a link with off-line approaches [8], without their time-consuming drawbacks. An optimal reference trajectory is hence deduced from the nonlinear model (Section III), in order to minimize the control efforts.

A state space representation is then inherited from the forces balance model (Section IV), so as to synthesize a backstepping control law (Section V). To our knowledge, most of feedback controller schemes designed in the scope of microrobotics facing drag are PID approaches [7], [9]. Authors report instabilities and important oscillations around the equilibrium, especially when the blood stream is modeled as a pulsatile flow. They also indicate a lack of robustness to noise and unmodeled dynamics. In this paper, the control design is based on the backstepping approach we have recently developed in [10], which ensures Lyapunov stability. Since backstepping can be regarded as a pre-compensation of the model's nonlinearities, working with a more accurate model is a real improvement of our previous work. Some simulations results illustrate the strengths and limitations of the overall study (Section VI). Lastly we sum up results and discuss prospects (Section VII).

II. MODELING: FORCES BALANCE

The purpose of this section is to present a 2D state space model of a ferromagnetic microrobot of radius r immersed in blood vessel. The model encompasses the different forces that affect the robot's motion as well as its interaction with the vessel wall. The translational and rotational motions of the robot are expressed by:

$$\begin{cases} m\frac{d\vec{v}}{dt} = \vec{F}_m + \vec{F}_d + \vec{W}_a + \vec{F}_c + \vec{F}_{vdw} + \vec{F}_e \\ J\frac{d\vec{w}}{dt} = \vec{T}_m + \vec{T}_d + \vec{M}_c \end{cases} \quad (1)$$

where $\vec{v}$ and $\vec{w}$ are, respectively, the translational and rotational velocity of the robot, m and J its mass and moment of inertia. $\vec{F}_m$, $\vec{F}_d$, $\vec{W}_a$, $\vec{F}_c$, $\vec{F}_{vdw}$ and $\vec{F}_e$ respectively denote the magnetic force produced by the MRI gradient coils ($\vec{F}_m$), blood hydrodynamic drag force ($\vec{F}_d$), apparent weight ($\vec{W}_a$), the robot-to-wall contact force ($\vec{F}_c$), the Van der Waals force ($\vec{F}_{vdw}$) and the electrostatic force ($\vec{F}_e$). $\vec{T}_m$, $\vec{T}_d$ and $\vec{M}_c$ denote respectively the magnetic torque, hydrodynamic drag torque and the robot-to-wall contact moment.

In the rest of this paper, we assume that the orientation of the robot does not change due to the magnetic torque which tends to align the magnetization of the robot along the external field. $\vec{T}_d$ and $\vec{M}_c$ are much smaller order than $\vec{T}_m$.

To determine whether statistical mechanics or continuum mechanics formulations of fluid dynamics should be used, we refer to the dimensionless Knudsen number:

$$K_n = \frac{k_b T}{P \pi r^3 2^{5/2}} \tag{2}$$

where T, k_b and P respectively denote temperature, the Boltzmann constant and pressure. In our case, the low value $K_n \approx 10^{-13}$ ($\ll 10^{-3}$) ensures that the robot is large enough to neglect the effect of Brownian motion: the robot's motion is subjected to generic Navier-Stokes equations.

A. Magnetic force

The gradient coils of the MRI system provide magnetic gradients which produce a magnetic force F_m on the robot:

$$\vec{F}_m = \tau_m \mu_0 V (\vec{M}.\nabla)\vec{H} \tag{3}$$

where V is the robot's total volume, $\tau_m = \frac{V_m}{V}$ with V_m the ferromagnetic volume, $\vec{M}$ is the magnetization of the material, μ_0 is the permeability of free space, $\vec{H}$ is the external magnetic field and ∇ is the gradient operator.

B. Hydrodynamic drag force

The hydrodynamic drag force $\vec{F}_d$ exerting on a spherical body in an infinite extent of fluid is expressed as:

$$\vec{F}_d = -\frac{1}{2}\rho_f(\vec{v} - \vec{v}_f)^2_\infty A C_{d_\infty} \tag{4}$$

where $\vec{v} - \vec{v}_f$ denotes the relative velocity of the robot with respect to the fluid, A is the frontal area of the core and ρ_f is the density of the fluid. C_{d_∞} is the drag coefficient, a dimensionless quantity used to quantify the drag or resistance of an object in a fluid. C_{d_∞} is a function of the Reynolds number $Re_\infty = \frac{2r\rho_f|\vec{v}-\vec{v}_f|_\infty}{\eta}$; its expression for a spherical body in laminar flow is given by [11]:

$$C_{d_\infty} = \frac{24}{Re_\infty} + \frac{6}{1 + \sqrt{Re_\infty}} + 0.4 \tag{}$$

1) Non-Newtonian fluid: In case of blood, which exhibits a non-Newtonian behavior, the fluid's viscosity η is a function of vessel diameter d (in micron) and hematocrit rate h_d according to the three following empirical relationships [12]:

$$\eta = \frac{\eta_{plasma}d^2}{(d - 1.1)^2}\left[1 + \frac{(\eta_{0.45} - 1)d^2}{(d - 1.1)^2}\frac{(1 - h_d)^c - 1}{(1 - 0.45)^c - 1}\right]$$
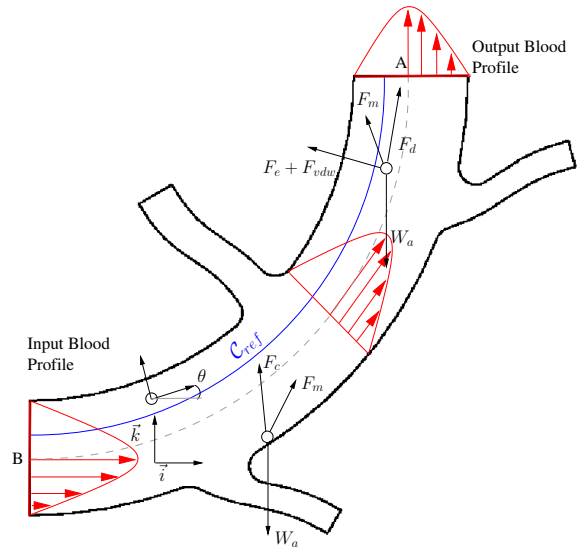

Fig. 1. Scheme of a blood vessel with minor bifurcations

with parameters η_{plasma} and $\eta_{0.45}$ denoting respectively the plasma's viscosity and the relative apparent blood viscosity for a fixed discharge hematocrit of 0.45, given by:

$$\eta_{0.45} = 6\, e^{-0.085d} + 3.2 - 2.44\, e^{-0.06d^{0.645}}$$

The shape of the viscosity dependance on hematocrit is:

$$c = \frac{10^{11}}{d^{12}} - (0.8 + e^{-0.075d})\left(\frac{d^{12}}{d^{12} + 10^{11}}\right)$$

2) Wall effects: For endovascular applications, influence of the vessel walls on the velocity of the robot has to be taken into account. In general, this wall effect is expressed as a ratio between the terminal relative velocity of the robot $(\vec{v} - \vec{v}_f)_t$ and its velocity $(\vec{v} - \vec{v}_f)_\infty$ in an infinite extent of fluid [13]:

$$\frac{|\vec{v} - \vec{v}_f|_t}{|\vec{v} - \vec{v}_f|_\infty} = \frac{1 + \left(\frac{\lambda}{\lambda_0}\right)^{\alpha_0}}{1 - \lambda^{\alpha_0}} \tag{5}$$

with ratio $\lambda = 2r/D$ and D denoting the vessel diameter (in meter). Parameters α_0 and λ_0 are functions of Reynolds number, but are commonly set to 1.5 and 0.29, respectively.

Thus, equation (4) is corrected as follows:

$$\vec{F}_d = -\frac{1}{2}\rho_f\left[\frac{1 - \lambda^{\alpha_0}}{1 + \left(\frac{\lambda}{\lambda_0}\right)^{\alpha_0}}(\vec{v} - \vec{v}_f)_t\right]^2 A C_{d_t} \tag{6}$$

Wall effects on the fluid in the vessel traditionally result in a parabolic profile of blood flow (see Figure 1). Besides, to fully take into account pulsatile flow caused by heart pumping in arteries, we consider a periodic deformation of the vessel's diameter $D(t)$ synchronized with $v_f(t)$.
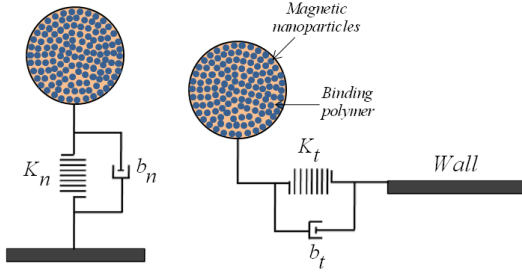
Fig. 2. Model of contact forces: robot-to-wall

C. Apparent weight

In addition to the magnetic and hydrodynamic forces, apparent weight (combined action of weight and buoyancy) is acting on the spherical robot:

$$\vec{W}_a = V(\rho - \rho_f)\vec{g} \qquad (7)$$

where $\rho = \tau_m \rho_m + (1 - \tau_m)\rho_{poly}$ with ρ_m and ρ_{poly} the magnetic material's and polymer's densities.

D. Contact force

The normal and tangential interaction between the robot and the wall are expressed by a Voigt model with the spring constant K and the decay coefficient of dashpot b, as shown in Figure 2, where indexes $\vec{n}$ and $\vec{t}$ indicate respectively the normal and tangential normalized vectors.

The normal component of the contact force $\vec{F}_{cn}$ acting on the robot is given by the sum of a non-linear elastic component and a linear viscous damping: [14]:

$$\vec{F}_{cn} = (K_n \delta^{3/2} + b_n \dot{\delta})\vec{n} \qquad (8)$$

where δ is the elastic deformation of the wall at the contact point and $\vec{n}$ is the normal unit vector pointing from the robot to the contact surface. The stiffness K_n can be calculated by Hertzian contact theory [15] as follows:

$$K_n = \frac{\frac{4\sqrt{r}}{3}}{\frac{1-\sigma_p^2}{E_p} + \frac{1-\sigma_w^2}{E_w}}$$

where E_p and E_w are the Young's modulus of robot and wall, and σ_p, σ_w are respectively the Poisson's ratios of robot and wall. The damping coefficient b_n is deduced from K_n using $b_n = 2\sqrt{mK_n}$.

The tangential component of the contact force takes part when the robot is rotating or in case of oblique collision with the wall:

$$\vec{F}_{ct} = (K_t \zeta + b_t \dot{\zeta})\vec{t} \qquad (9)$$

where ζ is the displacement in the tangential direction and $\vec{t}$ is the tangential unit vector. The stiffness K_t and damping coefficient b_t are given by:

$$K_t = \frac{8\sqrt{r}G_p}{2 - \sigma_p} \delta^{1/2} , \quad b_t = 2\sqrt{mK_t}$$

where G_p is the shear modulus related to the Young's modulus E_p and Poisson ratio σ_p, i.e. $G_p = \frac{E_p}{2(1+\sigma_p)}$.

E. Van der Waals and electrostatic forces

When the robot and the wall are not in contact, they interact each other through Van der Waals and electrostatic forces. These two interaction forces have different dominant regimes. In fact, when the robot is close to the wall, Van der Waals force is dominant. As the robot move away from the wall, the Van der Waals force rapidly decrease and the electrostatic force prevails.

The Van der Waals potential between the robot and the wall is given by [16]:

$$\vec{V}_{vdw} = -\frac{A_h}{6}\left(\frac{1}{H} + \frac{1}{2+H} + \ln\frac{h}{2+H}\right)\vec{n} \qquad (10)$$

where A_h is the Hamaker constant and $H = h/r$ is normalized distance between the robot and the wall. Then, the Van der Waals interaction force is given by differenciating (10) $\vec{F}_{vdw} = -\nabla \vec{V}_{vdw}$.

The electrostatic force between the robot and the wall considered as an uncharged surface is given by [17]:

$$\vec{F}_e = \frac{q^2}{4\pi\epsilon\epsilon_0(r+h)^2}\vec{n} \qquad (11)$$

with q the robot charge, ϵ the dielectric density of the medium in which the interaction occurs and ϵ_0 the vacuum permittivity. [18] gives the expression of the maximum allowable charge for a spherical body of radius r:

$$q(\mu C) = S \times Q = 4\pi r^2 \times 30(100r)^{-0.3}$$

III. MODELING: OPTIMAL TRAJECTORY

Previous forces balance gives us sufficient informations to plan an optimal trajectory. At least two cases A and B, shown on the Figure 1, should be considered. In the first one, the robot is in a vertical vessel and the magnetic force $\vec{F}_m$ should counter both contributions of the robot's apparent weight $\vec{W}_a$ and the drag force $\vec{F}_d$ when blood is flowing back (Curve A of Figure 3). The drag force decreases when the robot approaches the wall due to the parabolic profile of velocity. Thus the reference trajectory should be as near as possible to wall. In the second case, the robot is in a horizontal vessel and the magnetic force should counter contributions of the robot's apparent weight, electrostatic and Van der Waals forces, $\vec{F}_e$ and $\vec{F}_{vdw}$ (Curve B of Figure 3). This case shows that near the wall, $\vec{F}_e$ and $\vec{F}_{vdw}$, which point to the wall, are dominant and the magnetic force is no more sufficient to counter it. Nevertheless there is an optimal position where the sum of the two forces compensates perfectly the robot's weight. Moreover, the curve A shows that at this point, the magnetic force exceeds the drag force. From these observations, we define an optimal path as an arc passing through the point C.

IV. MODELING: STATE SPACE REPRESENTATION

Let (x, z) denote the position of the robot in the vessel with respect to a given frame $\mathcal{F}(O, \vec{i}, \vec{k})$. The state model is
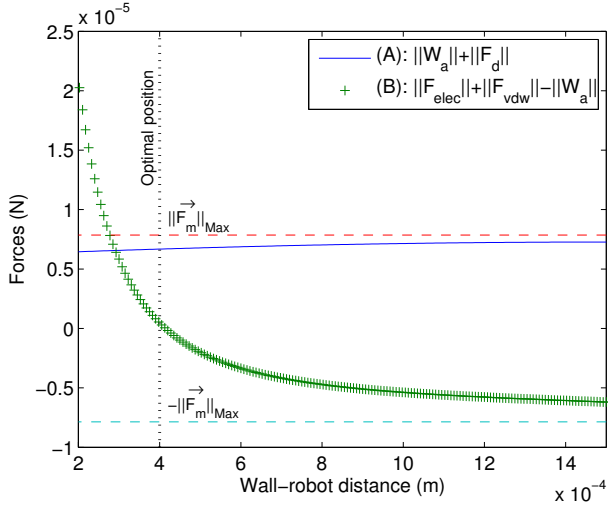
Fig. 3. Forces balances in vertical (A) and horizontal (B) artery

Fig. 4. Comsol results : Velocity profile in a blood vessel with minor bifurcations

established from differential equation (1) defining the robot's dynamic behavior, projected on $\vec{i}$ and $\vec{k}$ axes:

$$\begin{cases} m\ddot{x} = F_{m_x} + F_{d_x} + F_{cn_x} + F_{ct_x} + F_{vdw_x} + F_{e_x} \\ m\ddot{z} = F_{m_z} + F_{d_z} + W_a + F_{cn_z} + F_{ct_z} + F_{vdw_z} + F_{e_z} \end{cases} \quad (12)$$

where indexes x (respectively z) denote projections on $\vec{i}$ ($\vec{k}$).

Let x_1, x_2, x_3, x_4 denote respectively the particule's position and velocity along $\vec{i}$ axis, and the position and velocity along $\vec{k}$ axis. Assuming that positions x_1 and x_3 can be measured thanks to the MRI imaging system, let y denote the state's measure. Using expressions of forces given by (3), (6), (7), (8), (9), (11) and Van der Waals interaction derivated from potential (10), and adequate projection of local frame along the geometry of the vessel[1], system (12) can be written in the form:

$$(\mathcal{S}) \begin{cases} \dot{x}_1 & = & x_2 \\ \dot{x}_2 & = & f_2(x_1, x_2, x_3, x_4) + au_1 \\ \dot{x}_3 & = & x_4 \\ \dot{x}_4 & = & f_4(x_1, x_2, x_3, x_4) + au_2 \\ y & = & \begin{pmatrix} x_1 \\ x_3 \end{pmatrix} \end{cases} \quad (13)$$

where control inputs $u_1 = \nabla B_x$ and $u_2 = \nabla B_z$ are the magnetic gradients, parameter $a = \frac{\tau_m M}{\rho}$, and f_i are highly nonlinear functions of the full state.

V. CONTROL APPROACH

In this section, we present a control design for Lyapunov-stabilizing trajectories for system $(\mathcal{S})$. Since determination of Lyapunov functions is generically a challenging issue, it is preferable to use Lyapunov control functions in a backstepping control approach [19], [20]. Since this design requires a triangular form for the control system, we propose the following change of coordinates:

$$\begin{cases} X = \begin{pmatrix} x_1 \\ x_3 \end{pmatrix}; & Z = \begin{pmatrix} x_2 \\ x_4 \end{pmatrix}; & U = \begin{pmatrix} u_1 \\ u_2 \end{pmatrix} \end{cases} \quad (14)$$

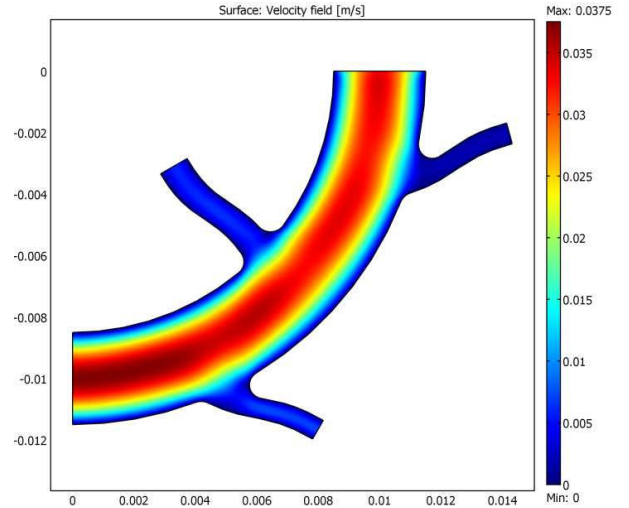[1]The drag force is not linearly distributed between $\vec{i}$ and $\vec{k}$ axis.

Thus, we obtain a new system in a triangular form:

$$(\mathcal{S}') \begin{cases} \dot{X} & = & Z \\ \dot{Z} & = & F(X, Z) + U \\ y & = & X \end{cases} \quad (15)$$

Denoting X_{ref}, $\dot{X}_{ref}$ and $\ddot{X}_{ref}$ respectively the desired reference trajectory, velocity and acceleration, the control law for system $(\mathcal{S}')$ can be expressed as [10]:

$$\begin{aligned} U & = & \ddot{X}_{ref} + (k_1 + k_2)\dot{X}_{ref} + (1 + k_1 k_2)X_{ref} \\ & & -(1 + k_1 k_2)X - (k_1 + k_2)Z - F(X, Z) \end{aligned} \quad (16)$$

where k_1 and k_2 are the strictly positive backstepping gains.

VI. SIMULATIONS

The robot is made of $\tau_m = 80\%$ NdFeB particles which has a combination of very high remanence and coercivity, and 20% of binding polymer. Simulations are performed by taking into account the limitations of a clinical MRI system. In order not to exceed the capacity of existing MRI systems, the applied control law (16) is now corrected as $\frac{u_i}{k(t)}$, with $k(t) = \max\left\{1, \frac{u_i}{u_{i,max}}\right\}$.

A pulsatile flow is included by imposing a time-varying velocity. As a first approximation of a physiological pulse, we use a time-sinusoidal profile with spatial parabolic form. In the case of artery, such an approximation leads to:

$$v_f(t) = 0.025(1 + 1.15\sin 2\pi t) \times \left[1 - \left(\frac{D/2 - h}{r}\right)^2\right]$$

Our studies assume the presence of minor bifurcations (see Figure 1). This geometry leads to only slight change in the velocity's profile and amplitude (see Figure 4). The developed controller must be sufficiently robust to compensate this effect which could be considered as a disturbance. Major bifurcations will require a further study
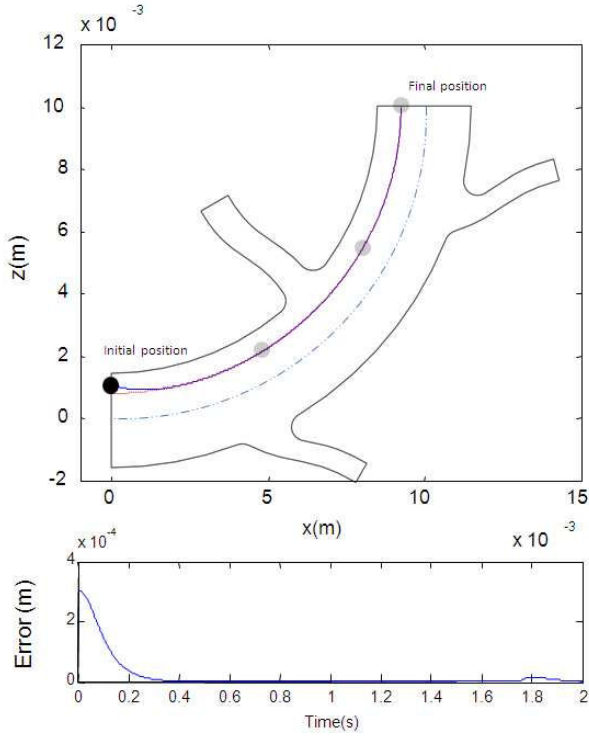
Fig. 5. (a) XZ trajectory : reference trajectory (red dotted) and real trajectory (blue solid line). (b) Tracking error (blue solid line).

of velocity's field profile.

In the following, the performances and stability of the controller with respect to noise measurement, physiological parameters variations and uncertainties are illustrated by two simulations, whose parameters are given in Table I. A first simulation is led so as to pinpoint robustness to model errors, and the second one to study sensitivity to output noise.

Simulation of Figures 5, 6 is performed by assuming that the blood's viscosity is affected by uncertainty of 50% of its nominal value and the vessel's diameter by uncertainty of 10%. This simulation shows that after a transient phase, the position tracking performance is robust enough to model's error (subfigure of Figure 5). Even though the optimal trajectory is computed so as to remain within MRI limitations, the matched uncertainties cause the control inputs to reach saturation: the MRI protection has priority over the tracking efficiency, which results in a degradation of the tracking error at $t = 1.75s$. It should be noticed that the tracking error tends to zero as soon as the input decreases under the saturation.

In a second simulation (Figures 7 and 8), we assume a white gaussian noise is applied on the position measurement. This noise is about 10% of the measured signal (about some hundred micrometers), which is motivated by the common precision of clinical MRI devices. Figure 7(b) illustrate that the controller is quite stable despite the noise, and does not
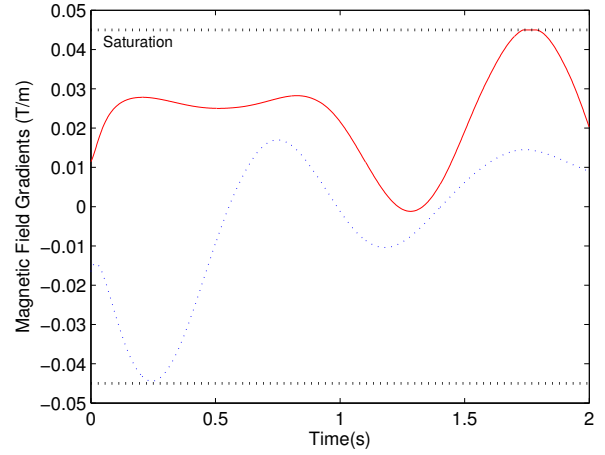

Fig. 6. Control input : magnetic field gradients on $\vec{i}$-axis (dotted) and on $\vec{k}$-axis (solid line)

TABLE I
SIMULATIONS DATA

Plasma's viscosity	η_{plasma}	5×10^{-3} $[Pa.s]$
Blood's density	ρ_f	1060 $[kg.m^{-3}]$
Robot's density	ρ_m	8000 $[kg.m^{-3}]$
Robot's radius	r	300 $[\mu m]$
Vessel's diameter	D	3 $[mm]$
Polymer's density	ρ_{poly}	1500 $[kg.m^{-3}]$
Ferromagnetic ratio	τ_m	0.8
Magnetization	M	1.95×10^{6} $[A.m^{-1}]$
Hematocrit	h_d	0.45
Robot's Young's modulus	E_p	10^{9} $[Pa]$
Wall's Young's modulus	E_w	0.75×10^{6} $[Pa]$
Robot's Poisson's ratio	σ_p	0.27
Wall's Poisson's ratio	σ_w	0.30
Hamaker constant	A_h	4×10^{-19} $[J]$
Blood's dielectric density	ε	77 $[C^2.N^{-1}.m^{-2}]$
Initial condition on x	x_0	$(0,0,0.0011,0)^T$
Inputs saturations	$u_{i,max}$	45 $[mT.m^{-1}]$
Controller gains	k_1	15
	k_2	30

even reach saturations (Figure 8). Nevertheless, Figure 7(a) shows that the trajectory tracking is sensitive to noise. We can expect that this drawback effect can be reduced using an observer. In addition to estimate some parameters like blood's velocity (assumed to be known in this paper), an observer will tend to smooth the output signals.

VII. CONCLUSION

In this paper, we have presented a highly nonlinear model for a MRI guided microrobot in blood vessels. This model takes into account the non-Newtonian behavior of blood, as well as wall effects and interactions. It makes it possible to hence deduce an optimal trajectory. Besides, we have developed a nonlinear control law based on the backstepping approach. Parameters uncertainties and noise effects have been illustrated by simulations. It appears that the system is robust to uncertain physiological parameters, but proved quite sensitive to output noise, though remains stable.
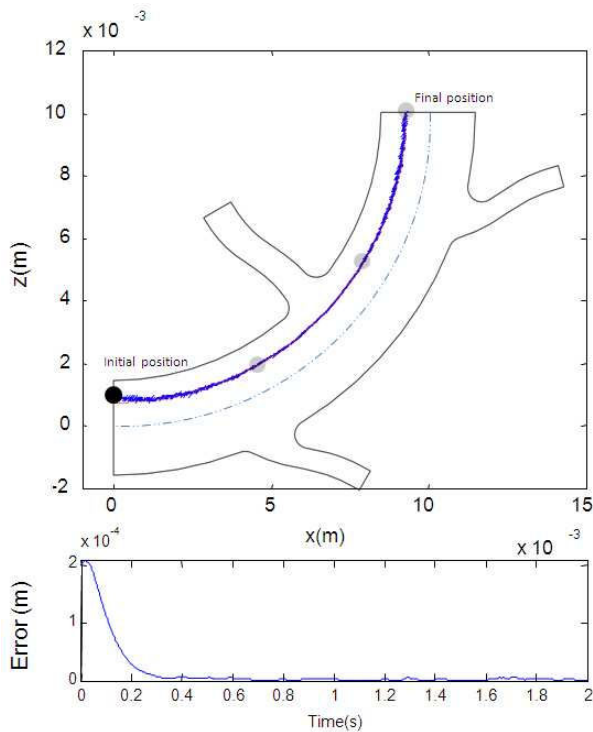
Fig. 7.   (a) XZ trajectory : reference trajectory (red dotted) and real trajectory (blue solid line). (b) Tracking error (blue solid line).
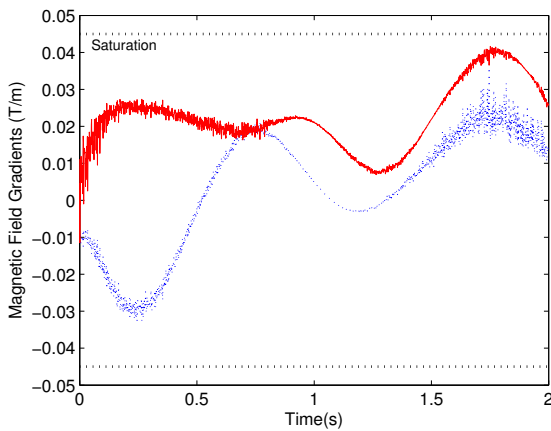

Fig. 8.   Control input : magnetic field gradients on $\vec{i}$-axis (dotted) and on $\vec{k}$-axis (solid line)

As stated in Section VI, system robustness to noise can be improved by implementing a high gain observer based on [10] but fitted for this more complete and complex model. We are also working on estimating the blood's velocity and frequency, assumed to be known at the moment, using Kazantis-Kravaris Luenberger observers [21]. Another decisive point for future in-vivo experiments will concern robustness to vessel's motions induced by heartbeat and respiration, which impact the geometry and position of the vessel. These perturbations should not be considered as noise, but rather as a matched uncertainty in a model including these phenomena. Additionnaly, the modeling of

impact of major bifurcations on the blood's velocity profile is underway.

VIII. ACKNOWLEDGMENTS

REFERENCES

[1] J. Abbott, Z. Nagy, F. Beyeler, and B. Nelson, "Robotics in the small: Part 1 microrobotics," *IEEE Robotics and Automation Magazine*, vol. 14, no. 2, pp. 92–103, June 2007.

[2] G. T. Gillies, R. C. Ritter, W. C. Broaddus, M. S. Grady, M. A. Howard, and R. G. McNeil, "Magnetic manipulation instrumentation for medical physics research," *Rev. of Sci. Instruments*, vol. 65, no. 3, March 1994.

[3] T. Honda, K. I. Arai, and K. Ishiyama, "Micro swimming mechanisms propelled by external magnetic fields," *IEEE Trans. on Magnetics*, vol. 32, no. 5, 1996.

[4] E. G. Quate, K. G. Wika, M. A. Lawson, G. T. Gillies, R. C. Ritter, M. S. Grady, and M. A. H. and, "Goniometric motion controller for the superconducting coil in amagnetic stereoaxis system," *IEEE Trans. on Biomed. Eng.*, vol. 38, no. 9, pp. 899–905, September 1991.

[5] S.-I. Takeda, F. Mishima, S. Fujimoto, Y. Izumi, and S. Nishijima, "Development of magnetically targeted drug delivery system using superconducting magnet," *Journal of Magnetism and Magnetic Materials*, 2006.

[6] J.-B. Mathieu, G. Beaudoin, and S. Martel, "Method of propulsion of a ferromagnetic core in the cardiovascular system through magnetic gradients generated by an mri system," *IEEE Trans. on Biomedical Engineering*, vol. 53, no. 2, pp. 292–299, 2006.

[7] S. Tamaz, R. Gourdeau, A. Chanu, J.-B. Mathieu, and S. Martel, "Real-time mri-based control of a ferromagnetic core for endovascular navigation," *IEEE Trans. on Biomed. Eng.*, vol. 55, no. 7, July 2008.

[8] P. Vartholomeos and C. Mavroidis, "Simulation platform for self-assembly structures in mri-based nanorobotic drug delivery systems," in *IEEE. Int. Conf. on Robotics and Automation*, May 2010, to be published.

[9] J. Mathieu and S. Martel, "In-vivo validation of a propulsion method for untethered medical microrobots using a clinical magnetic resonance imaging system," in *IROS*, 2007, pp. 502–508.

[10] L. Arcese, M. Fruchard, and A. Ferreira, "Nonlinear modeling and robust controller-observer for a magnetic microrobot in a fluidic environment using mri gradients," *IEEE International Conference on Intelligent Robots and Systems*, pp. 534–539, 2009.

[11] F. White, *Viscous Fluid Flow*.   McGraw Hill New-York, 1991.

[12] A.-R. Pries, T.-W. Secomb, and P. Gaehtgens, "Biophysical aspects of blood flow in the microvasculature," *Cardiovascular Research*, vol. 32(4), pp. 654–667, 1996.

[13] R. Kehlenbeck and R. D. Felice, "Empirical relationships for the terminal settling velocity of spheres un cylindrical columns," *Chemical Eng. Technology*, vol. 21, pp. 303–308, 1999.

[14] E. Tijskens, H. Ramon, and J.-D. Baerdemaeker, "Discret element modelling for process simulation in agriculture," *Journal of Sound and Vibration*, vol. 266, pp. 493–514, 2003.

[15] Y. Tsuji and T. Tanaka, T. Ishida, "Lagragian numerical simulation of plug flow of cohesionless particles in a horizontal pipe," *Powder Technology*, vol. 71, pp. 239–250, 1992.

[16] K. Iimura, S. Watanabe, M. Suzuki, M. Hirota, and K. Higashitani, "Simulation of entrainment of agglomerates from plate surfaces by shear flows," *Chemical Engineering Science*, vol. 64, pp. 1455–1461, 2009.

[17] D. Hays, "Electrostatic adhesion of non-uniformly charged dielectric sphere," *Int. Phys. Conf. ser.*, vol. 118, p. 223228, 1991.

[18] ——, *Role of Electrostatics in Adhesion, in Fundamentals of Adhesion*, L.-H. Lee, Ed.   PLENUM PRESS, 1991.

[19] M. Krstić, I. Kanellakopoulos, and P. Kokotović, *Nonlinear and Adaptative Control Design*.   John Wiley & Sins, Inc., New York, 1995.

[20] I. Kanellakopoulos, P. Kokotović, and A. Morse, "A toolkit for nonlinear feedback design," *SCL*, vol. 18, pp. 83–92, 1992.

[21] V. Andrieu and L. Praly, "On the existence of a kazantis-kravaris / luenberger observer," *SIAM*, vol. 45, no. 2, pp. 432–456, 2006.